

Article

Garcinia mangostana L. Leaf-Extract-Assisted Green Synthesis of CuO, ZnO and CuO-ZnO Nanomaterials for the Photocatalytic Degradation of Palm Oil Mill Effluent (POME)

Yu Bin Chan ¹, Mohammad Aminuzzaman ^{1,2}, Yip Foo Win ¹, Sinouvassane Djearamane ^{3,4}, Ling Shing Wong ^{5,*}, Samar Kumar Guha ⁶, Hamad Almohammadi ⁷, Md. Akhtaruzzaman ^{8,9,*} and Lai-Hock Tey ^{1,*}

- ¹ Department of Chemical Science, Faculty of Science, University Tunku Abdul Rahman (UTAR), Kampar Campus, Jalan University, Bandar Barat, Kampar 31900, Perak, Malaysia; yubinchan1221@gmail.com (Y.B.C.); mohammoda@utar.edu.my (M.A.); yipfw@utar.edu.my (Y.F.W.)
- ² Centre for Advanced and Sustainable Materials Research (CASMR), University Tunku Abdul Rahman (UTAR), Sungai Long 43000, Selangor, Malaysia
- ³ Department of Allied Health Science, Faculty of Science, University Tunku Abdul Rahman (UTAR), Kampar Campus, Jalan University, Bandar Barat, Kampar 31900, Perak, Malaysia; sinouvassane@utar.edu.my
- ⁴ Biomedical Research Unit and Lab Animal Research Centre, Saveetha Institute of Medical and Technical Sciences, Saveetha Dental College, Saveetha University, Chennai 60210, India
- ⁵ Faculty of Health and Life Sciences, INTI International University, Nilai 71800, Negeri Sembilan, Malaysia
- ⁶ Department of Arts and Sciences, Faculty of Engineering, Ahsanullah University of Science and Technology, 141-142, Love Road, Tejgaon I/A, Dhaka 1208, Bangladesh; skguha.as@aust.edu
- ⁷ Department of Chemical Engineering, Faculty of Engineering, Islamic University of Madinah, Madinah 42351, Saudi Arabia; hha@iu.edu.sa
- ⁸ Department of Chemistry, Faculty of Science, Islamic University of Madinah, Madinah 42351, Saudi Arabia
- ⁹ Sustainable Research Center, Islamic University of Madinah, Madinah 42351, Saudi Arabia
- * Correspondence: lingshing.wong@newinti.edu.my (L.S.W.); makhtar@iu.edu.sa (M.A.); teylh@utar.edu.my (L.-H.T.)



Citation: Chan, Y.B.; Aminuzzaman, M.; Win, Y.F.; Djearamane, S.; Wong, L.S.; Guha, S.K.; Almohammadi, H.; Akhtaruzzaman, M.; Tey, L.-H. *Garcinia mangostana* L. Leaf-Extract-Assisted Green Synthesis of CuO, ZnO and CuO-ZnO Nanomaterials for the Photocatalytic Degradation of Palm Oil Mill Effluent (POME). *Catalysts* **2024**, *14*, 486. <https://doi.org/10.3390/catal14080486>

Academic Editor: Natalia Martinsovich

Received: 10 July 2024

Revised: 23 July 2024

Accepted: 24 July 2024

Published: 29 July 2024



Copyright: © 2024 by the authors. Licensee MDPI, Basel, Switzerland. This article is an open access article distributed under the terms and conditions of the Creative Commons Attribution (CC BY) license (<https://creativecommons.org/licenses/by/4.0/>).

Abstract: The treatment of palm oil mill effluent (POME) poses a significant challenge for Malaysia's palm oil industry, necessitating compliance with the Department of Environment (DOE) regulations prior to discharge. This study introduces an eco-friendly synthesis method utilizing mangosteen (*Garcinia mangostana* L.)-leaf aqueous extract to fabricate copper oxide (CuO), zinc oxide (ZnO) nanoparticles (NPs), and their nanocomposite (CuO-ZnO NCs). The physicochemical properties of these nanomaterials were characterized using various analytical tools and their effectiveness in reducing the chemical oxygen demand (COD) of palm oil mill effluent (POME) was assessed under the illumination of two types of light sources: monochromatic blue- and polychromatic white-light emitting diodes (LEDs). CuO-ZnO NCs demonstrated superior performance, with the lowest energy bandgap (1.61 eV), and achieved a COD removal efficiency of $63.27\% \pm 0.010$ under blue LED illumination, surpassing the DOE's discharge limit of 100 mg/L. This study offers a cost-effective and environmentally friendly method for synthesizing heterojunction materials, which show great potential as photocatalysts in reducing POME COD to permissible levels for discharge.

Keywords: green synthesis; nanomaterials; wastewater treatment; palm oil mill effluent (POME); photodegradation; chemical oxygen demand (COD)

1. Introduction

Palm oil mill effluent (POME), the wastewater generated during the final stage of palm oil production, presents a significant environmental challenge [1]. Characterized by its dark, viscous nature, unpleasant odor, acidic pH (3.5–4.2) and brown color due to a mix of liquids, residual oils and suspended solids, POME is a complex mixture [2,3]. Its brownish hue results from a high concentration of phenolic compounds, pectin, tannin, carotene, and lignin, alongside substantial amounts of inorganic minerals, organic acids,

carbohydrates and amino acids. Comprising approximately 95% water, with the remainder being oil, suspended solids, and dissolved solids, untreated POME is a potent pollutant with a chemical oxygen demand (COD) ranging from 15,000 to 100,000 mg/L [4–9]. Consequently, direct discharge of POME into aquatic ecosystems severely depletes oxygen levels, rendering them inhospitable to aquatic life [2,3,10].

Traditionally, the open ponding system has been employed in Malaysia for POME treatment. However, this method is laborious, space-intensive, and inadequately mineralizes highly polluted water [11]. Moreover, even treated POME may still adversely affect the environment. Consequently, there is an urgent need for innovative solutions to degrade POME more effectively, such as the utilization of photocatalysts [12].

Photocatalysts, particularly metal oxide heterogeneous photocatalysts, offer a promising avenue for organic pollutant removal during wastewater treatment [13–15]. Advanced oxidative processes (AOPs), employing photocatalysts, have emerged as efficient, practical, and environmentally friendly methods for mineralizing organic compounds [10]. Notably, hydroxyl radicals ($\text{HO}\bullet$) generated during AOPs facilitate the redox conversion of organic molecules into simpler compounds, including carbon dioxide and water, within a few hours, without generating secondary waste products [9,15,16]. While various chemical-based materials, including metal oxides, have been utilized for pollutant removal [10], the wide energy bandgap of individual semiconductors limits their efficacy as photocatalysts in wastewater treatment [15].

Copper oxide (CuO) and zinc oxide (ZnO) stand out as notable semiconductors in this context. CuO, a non-toxic *p*-type semiconductor, possesses a low bandgap (1.20–2.00 eV) and distinctive electrical, magnetic, and optical properties [14,17–23]. Meanwhile, ZnO, an *n*-type semiconductor, boasts a wide bandgap energy (3.30–3.37 eV), high exciton binding energy (60 meV), and excellent chemical, photo-, and thermal stability [14,20,21]. Despite their individual merits, CuO suffers from rapid electron–hole (e^-/h^+) pair recombination [14], while ZnO's broad bandgap necessitates UV light for photo-degradation, limiting its efficiency under visible light. Additionally, ZnO is prone to photo-corrosion and exhibits a low capacity for visible light absorption, necessitating modification to enhance its photo-responsiveness [6,14,19,20,24].

In designing low-energy bandgap heterojunction nanomaterials, impurity addition to individual semiconductors is crucial [19], as it facilitates favorable e^-/h^+ pair separation, thereby enhancing photo-catalysis [15,19]. Compared to single semiconductor metal oxide nanoparticles (NPs), the mixing of semiconductors offers superior properties, making them highly applicable in various technologies [18,21]. Notably, *p-n* heterojunction nanocomposites (NCs) exhibit homogeneous size distribution [17], increased surface area [18], and enhanced light response at visible light range [14], making them ideal for environmental remediation. Among *p-n* type heterojunction semiconductors, CuO-ZnO NCs have garnered significant attention due to the effective electron transfer between CuO and ZnO, resulting in improved photocatalytic activity [14,20].

While many studies have investigated conventional methods for synthesizing nanomaterials for POME treatment under polychromatic light sources, the focus on COD removal efficiency under different spectral regions remains limited. Monochromatic blue light, with photon energy suitable for nanomaterial excitation, presents an intriguing avenue for enhancing photo-degradation efficiency. In this study, we synthesized pure CuO NPs, pure ZnO NPs, and CuO-ZnO NCs using a green approach involving mangosteen-leaf aqueous extract. We characterized their physicochemical properties and evaluated their efficacy in POME photodegradation under blue and white LEDs, representing mono- and polychromatic visible light sources, respectively. Finally, we elucidated the photo-degradation mechanism of CuO-ZnO NCs *p-n* heterojunction.

By bridging the gap in understanding the influence of spectral regions on COD removal efficiency and elucidating the mechanisms underlying CuO-ZnO NCs' photocatalytic activity, this study contributes to the development of efficient and sustainable approaches for POME treatment.

2. Results

The physicochemical properties of CuO NPs, ZnO NPs and CuO-ZnO NCs synthesized by mangosteen-leaf aqueous extract are compared in Table 1. The comparison with the physicochemical properties of green-synthesized CuO-ZnO NCs from other studies is summarized in Table 2. Meanwhile, Table 3 shows the COD removal efficiency by the synthesized CuO NPs, ZnO NPs and CuO-ZnO NCs under blue and white LEDs, respectively.

Table 1. Physicochemical properties of mangosteen-leaf aqueous extract-mediated CuO NPs, ZnO NPs and CuO-ZnO NCs.

Synthesized Nanomaterials	FT-IR (cm ⁻¹)					XRD			FE-SEM		UV-Vis
	$\nu(\text{O-H})$	$\nu(\text{C=C})$	$\nu(\text{-CH}_3)$	$\nu(\text{C-O-C})$	$\nu(\text{M-O})$ *	Average Crystalline Size (nm)	Dislocation Density ($\times 10^{14} \text{ cm}^{-1}$)	Micro Strain ($\times 10^{-4}$)	Average Particle Size (nm)	Morphology	Energy Bandgap (eV)
CuO NPs	3393	1636	1383	1094	537	24.42	16.77	1.46	116.27	Spherical	3.23
ZnO NPs	3458	1634	1383	1113	514	22.66	19.47	1.56	54.95	Spherical	2.52
CuO-ZnO NCs	3466	1633	1384	1098	540	29.04	11.86	1.25	82.32	Spherical	1.61

* Metal oxide band vibration.

Table 2. Comparison of physicochemical properties of CuO-ZnO NCs synthesized using various plant extracts in other studies.

Plants	Calcination Temperature (°C)	Energy Bandgap (eV)	Average Crystalline Size (nm)	Average Particle Size (nm)	Morphology	References
<i>Coriandrum sativum</i> (leaf)	350	-	11.30	11.00	Irregular	[18]
<i>Annona glabra</i> (leaf)	500	1.32–3.06	22.46–27.21	16.13–35.19	Spherical	[21]
<i>Zingiber officinale</i> (rhizome)	-	2.58–2.76	18.41–20.50	-	-	[22]
<i>Dovyalis caffra</i> (leaf)	400	-	23.21	20.00–32.00	Spherical	[25]
<i>Verbascum sinaiticum</i> (leaf)	500	2.74	18.00	-	Plate	[26]
<i>G. mangostana</i> (leaf)	600	1.61	29.04	82.32	Spherical	Current study

Table 3. COD removal efficiency in POME using mangosteen-leaf aqueous extract-mediated CuO NPs, ZnO NPs and CuO-ZnO NCs under blue and white LEDs, respectively.

Synthesized Nanomaterials	LEDs	COD Removal Efficiency (Means \pm SD)
CuO NPs	Blue	39.81 \pm 0.016
	White	40.14 \pm 0.025
ZnO NPs	Blue	43.85 \pm 0.010 ¹
	White	44.02 \pm 0.017 ¹
CuO-ZnO NPs	Blue	63.27 \pm 0.010
	White	35.77 \pm 0.017

¹ Significant at $p < 0.05$.

2.1. Physicochemical Properties

In Figure 1, 3393–3466 cm⁻¹ and 1633–1636 cm⁻¹ correspond to $\nu(\text{O-H})$ stretching and $\nu(\text{C=C})$ stretching, respectively. In addition, 1383–1384 cm⁻¹ and 1094–1113 cm⁻¹ correspond to $\nu(\text{C-H}_3)$ bending and $\nu(\text{C-O-C})$ stretching, respectively. On the other hand, the stretching mode of $\nu(\text{M-O})$ in synthesized nanomaterials was located at 514–540 cm⁻¹. The $\nu(\text{M-O})$ of CuO-ZnO NCs was located at a higher frequency (540 cm⁻¹) than CuO NPs (537 cm⁻¹) and ZnO NPs (514 cm⁻¹). The calculated $\nu(\text{M-O})$ detected in synthesized CuO NPs (Figure 1a) and ZnO NPs (Figure 1b) were 814 and 813 cm⁻¹, respectively, higher than the corresponding experimental values of 537 and 514 cm⁻¹. Similarly, $\nu(\text{M-O})$ frequency in CuO-ZnO NCs was 814 cm⁻¹ higher than the experimental band location at 540 cm⁻¹ (Figure 1c).

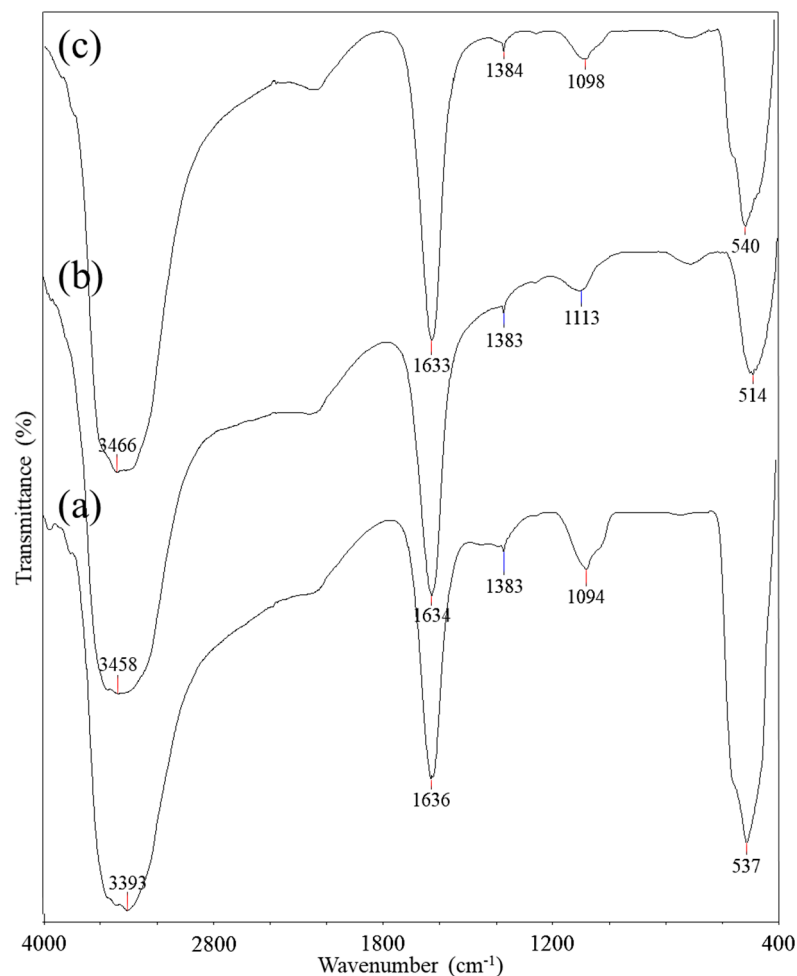


Figure 1. FT–IR spectra of mangosteen-leaf aqueous extract-mediated synthesized (a) CuO NPs, (b) ZnO NPs and (c) CuO-ZnO NCs.

The synthesized CuO NPs were in good agreement with the monoclinic-tenorite phase, with the $C_{2/c}$ space group matched with ICDD 00-045-0937 having the 2θ values of 32.40° , 35.41° , 38.62° , 48.64° , 61.44° , 66.13° and 68.00° , and indexed as $(-1\ 1\ 0)$, $(0\ 0\ 2)$, $(1\ 1\ 1)$, $(-2\ 0\ 2)$, $(-1\ 1\ 3)$, $(0\ 2\ 2)$ and $(-2\ 2\ 0)$, respectively (Figure 2a), with a purity of 93.5%. In Figure 2b, the hexagonal-zincite phase with a P_{63mc} space group of ZnO NPs was synthesized has the diffraction peaks at 2θ values of 31.77° , 34.40° , 36.26° , 47.50° , 56.60° , 62.88° , 67.88° and 69.08° , indexed as $(1\ 0\ 0)$, $(0\ 0\ 2)$, $(1\ 0\ 1)$, $(1\ 0\ 2)$, $(1\ 1\ 0)$, $(1\ 0\ 3)$, $(1\ 1\ 2)$ and $(2\ 0\ 1)$, respectively, matched with ICDD 01-079-9878, with a purity of 95.5%. The synthesized CuO-ZnO NCs (Figure 2c) are composed of monoclinic-tenorite (61.2%) and hexagonal-zincite (32.9%) phases. The synthesized CuO-ZnO NCs have the CuO Miller indexes at the 2θ values of 32.47° , 35.40° , 38.63° , 48.54° , 61.41° , 66.00° and 67.78° , and the ZnO Miller indexes at the 2θ values of 31.46° , 34.30° , 36.11° , 47.34° , 56.46° , 62.68° , 66.00° and 68.97° , respectively. The average crystalline size of synthesized CuO-ZnO NCs was found to be the largest (29.04 nm), compared to synthesized CuO NPs (24.42 nm) and ZnO NPs (22.66 nm). In contrast, the dislocation density and micro strain of the synthesized nanomaterials were inversely related to the average crystalline size obtained. The dislocation density of synthesized ZnO NPs was $19.47 \times 10^{14}\ \text{cm}^{-1}$, followed by synthesized CuO NPs ($16.77 \times 10^{14}\ \text{cm}^{-1}$) and CuO-ZnO NCs ($11.86 \times 10^{14}\ \text{cm}^{-1}$). Likewise, the greatest micro strain was synthesized ZnO NPs (1.56×10^{-4}), followed by synthesized CuO NPs (1.46×10^{-4}), and the smallest was CuO-ZnO NCs 1.25×10^{-4} .

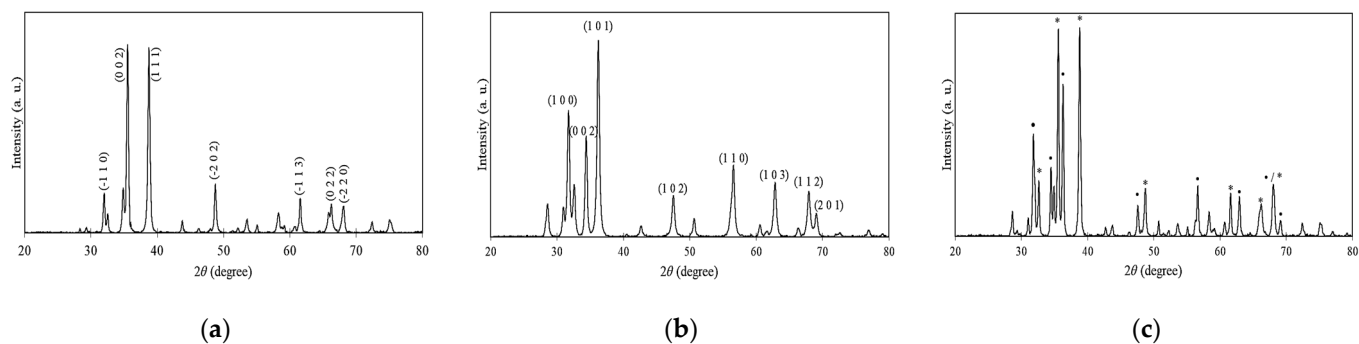


Figure 2. XRD patterns of mangosteen-leaf aqueous extract-mediated synthesized (a) CuO NPs, (b) ZnO NPs and (c) CuO-ZnO NCs. Note that ‘•’ denotes ZnO and ‘*’ denotes for CuO in CuO-ZnO NCs.

The average particle size of synthesized CuO NPs, ZnO NPs and CuO-ZnO NCs (Table 1) was 116.27, 54.95 and 82.32 nm, respectively, with shown great difference shown between XRD and FE-SEM measurements. FE-SEM micrographs (Figure 3) confirmed that the synthesized nanomaterial existed in a spherical shape in aggregation, with smooth and clear boundaries. Interestingly, the porous formation was observed in the synthesized ZnO NPs. In HR-TEM images (Figure 4), CuO-ZnO NCs were mostly spherical in shape, with a mean particle size of $45.44 \text{ nm} \pm 15.839$.

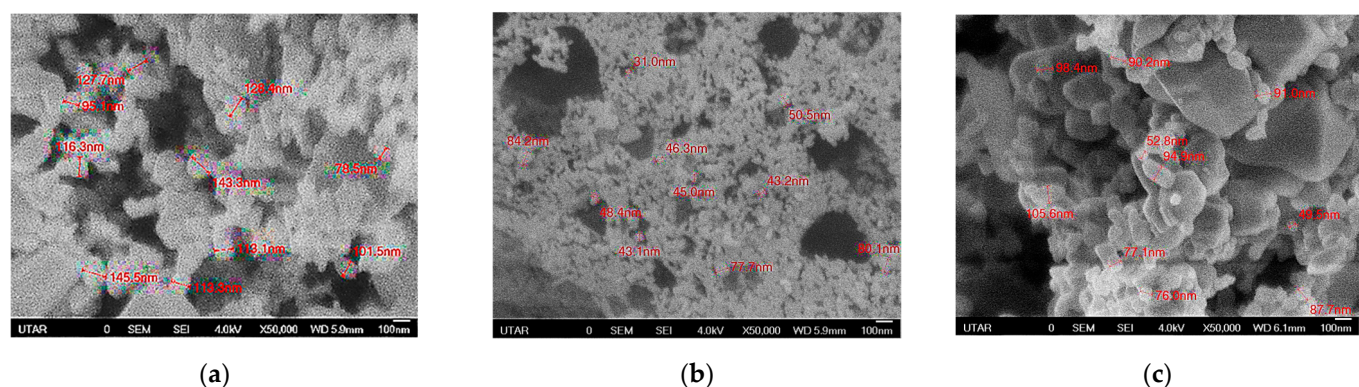


Figure 3. FE-SEM micrographs of mangosteen-leaf aqueous extract-mediated synthesized (a) CuO NPs, (b) ZnO NPs and (c) CuO-ZnO NCs.

EDX spectra of synthesized nanomaterials (Figure 5) show the appearance of a carbon weak signal located at 0.25 keV. As shown in Table 1, the weight percentages of carbon, oxygen, and copper in the synthesized CuO NPs were 33.14, 31.45, and 35.41%, respectively. Meanwhile, the synthesized ZnO NPs had the largest weight percentage of carbon, 46.24%, followed by oxygen (29.93%) and zinc (23.83%). Conversely, the weight percentage of the copper-to-zinc ratio found in the synthesized CuO-ZnO NCs was 1.40, which was comparable to the $\text{Cu}(\text{NO}_3)_2 \cdot 3\text{H}_2\text{O}$ and $\text{Zn}(\text{NO}_3)_2 \cdot 6\text{H}_2\text{O}$ added during the green synthesis. The weight percentages of carbon and oxygen were 28.96 and 38.69%, respectively.

Figure 6 shows the UV-Vis spectra and energy bandgap of mangosteen-leaf aqueous extract-mediated synthesized CuO NPs, ZnO NPs and CuO-ZnO NCs. The absorption peak of synthesized CuO NPs, ZnO NPs and CuO-ZnO NCs was detected at 398, 368 and 362 nm, respectively. The synthesized nanomaterials’ energy bandgaps were best fitted with direct transition $[(\alpha h\nu)^2 \text{ versus } h\nu]$. From this study, the energy bandgap was found to be largest in CuO NPs (3.23 eV), followed by ZnO NPs (2.52 eV), and the smallest was in CuO-ZnO NCs (1.61 eV).

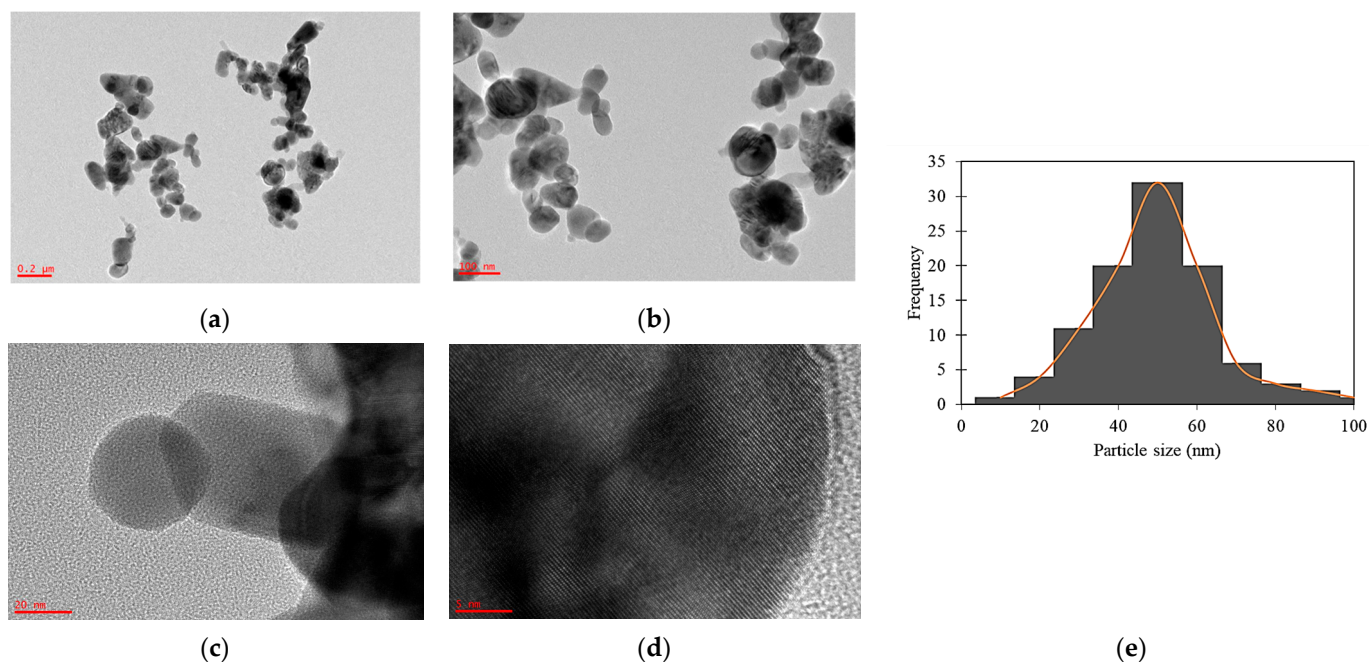


Figure 4. HR-TEM micrographs of mangosteen-leaf aqueous extract-mediated synthesized CuO-ZnO NCs under (a) 15,000 magnification, (b) 30,000 magnification, (c) 200,000 magnification, and (d) 800,000 magnification (the atoms of the CuO-ZnO NCs are represented by the small dots in the particle). (e) Histogram of particle size distribution.

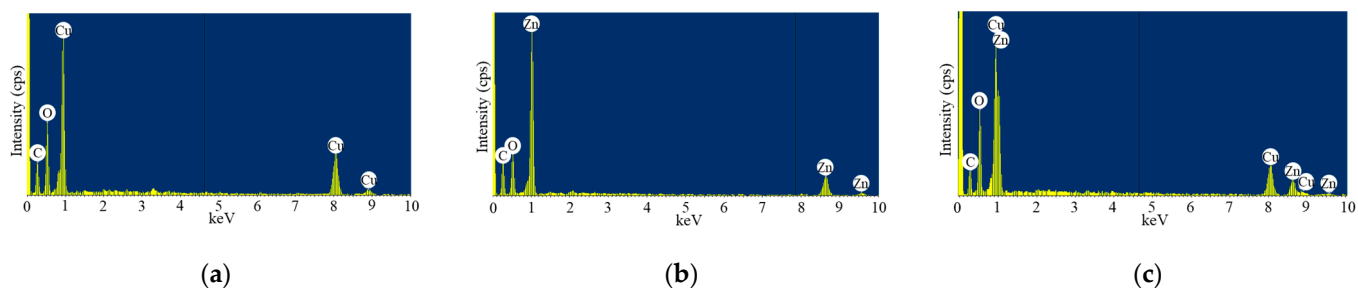


Figure 5. EDX spectra of mangosteen-leaf aqueous extract-mediated synthesized (a) CuO NPs, (b) ZnO NPs and (c) CuO-ZnO NCs.

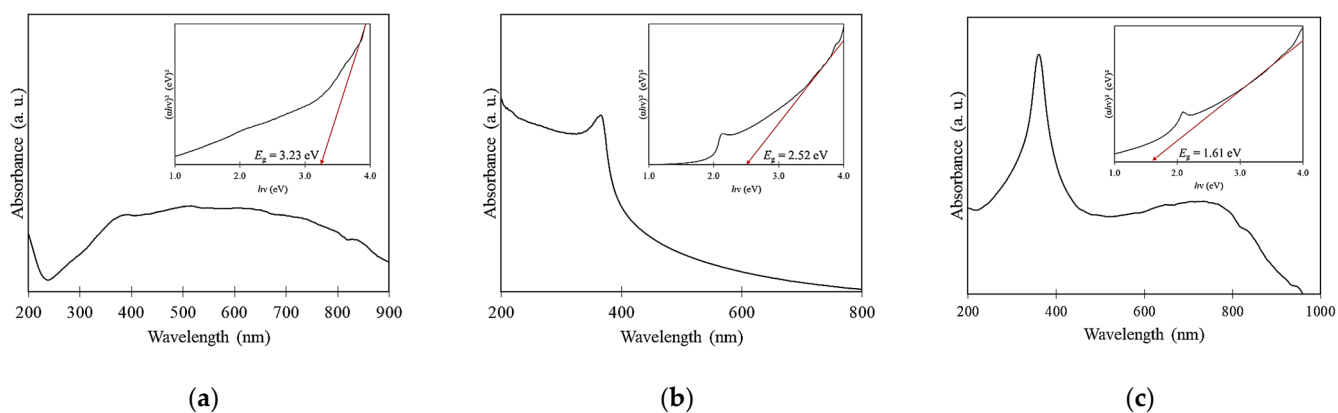


Figure 6. UV-Vis spectra and energy bandgap (using Tauc's plot approach) of mangosteen-leaf aqueous extract-mediated synthesized (a) CuO NPs, (b) ZnO NPs and (c) CuO-ZnO NCs.

2.2. COD Removal Efficiency

Under monochromatic blue LED (Figure 7), the synthesized CuO-ZnO NCs exhibited the highest COD removal efficiency ($63.27\% \pm 0.010$) and the treated POME's COD value ($75.67 \text{ mg/L} \pm 2.517$) was below the limit set by the Department of Environment in Malaysia, at 100.00 mg/L [27]. The COD removal efficiency of synthesized CuO NPs and ZnO NPs was $39.81\% \pm 0.016$ and $43.85\% \pm 0.010$, respectively. A comparatively low COD removal efficiency was recorded using synthesized CuO-ZnO NCs, CuO NPs and ZnO NPs under polychromatic white LED, recording $35.77\% \pm 0.017$, $40.14\% \pm 0.025$ and $44.02\% \pm 0.017$, respectively (Figure 7). Interestingly, a similar COD removal efficiency of synthesized CuO NPs and ZnO NPs was recorded under monochromatic blue and polychromatic white LEDs.

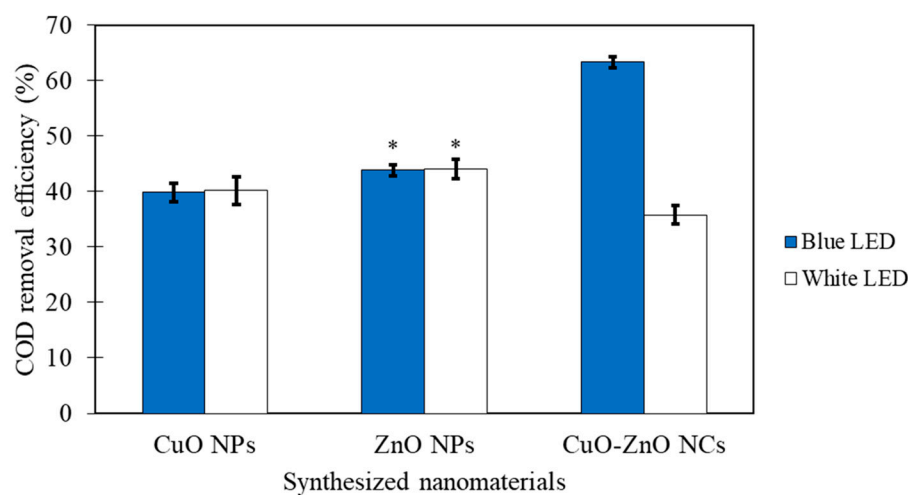


Figure 7. COD removal efficiency of mangosteen-leaf aqueous extract-mediated synthesized CuO NPs, ZnO NPs and CuO-ZnO NCs under blue (monochromatic) and white (polychromatic) LEDs. Note that * is significant at $p < 0.05$.

3. Discussion

The functional groups on the surface of synthesized nanomaterials were determined by FT-IR spectroscopy [22]. The detected functional groups on synthesized nanomaterials' surface came from mangosteen-leaf aqueous extract's phytochemicals, such as xanthenes, flavonoids and terpene [13,28–31]. The phytochemicals play a vital role during the green synthesis of nanomaterials as capping, stabilizing and reducing agents [30,32,33]. The $\nu(\text{M-O})$ location of synthesized nanomaterials was supported by other studies [18,21,22]. Generally, the metal oxide bands were located at the fingerprint region (below 1000 cm^{-1}), caused by interatomic vibrations [21]. Despite having a larger molecular mass than pure nanomaterials, CuO-ZnO NCs may have a density comparable to pure CuO NPs and which is less dense than pure ZnO NPs. The experimental values were different from calculated frequencies, due to the presence of resonance, hybridization [34], electron correlation effects and basis set deficiencies [35] in nanomaterials. In Figure 1b, the sharp $\nu(\text{M-O})$ indicated a strong wurtzite single phase of synthesized ZnO NPs [36]. Overall, the slight shifting of peaks in synthesized CuO-ZnO NCs (Figure 1c) was due to structural changes after the incorporation of ZnO within CuO [37].

Despite the exact route(s) of synthesis nanomaterials being based on phytochemicals, it is hypothesized that nanomaterials are green-synthesized via bio-reduction. Three stages are involved in green synthesizing nanomaterials through bio-reduction: (1) activation, (2) growth and (3) the termination phase. During the activation step, Cu^{2+} and Zn^{2+} are released from their own precursors when dissolved in mangosteen-leaf aqueous extract. The metal divalent ions form metal complexes with the phytochemicals [38,39] through hydrogen bonding and electrostatic attraction forces [13]. Consequently, the metal divalent

ions decrease to metallic form, indicated by the rapid color change in mangosteen leaf extract after the addition of precursors. They would be instantly oxidized to metal oxide nanomaterials during the calcination process by the oxygen from the atmosphere or the breakdown of phytochemicals which attach themselves to the metals by electrostatic attraction, resulting in nanomaterials before the development and stabilization phase because of the increased chemical reactivity of the exposed nanoscale metal surface. Throughout the growth and termination stages, the remaining phytochemicals in mangosteen-leaf aqueous extract would cause the metal oxide nanomaterials to aggregate and stabilize [38,40]. The literature also reported that the smaller nearby particles adhere to low-energy faces and crystallize to produce bigger, thermodynamically stable nanomaterials, due to the occurrence of Ostwald ripening. The adsorbed phytochemicals interact with the metal complex crystals' facets to produce certain crystal facets that have reduced surface tension and interfacial energy. As a result, the adsorbed phytochemicals alter the surface characteristics of the crystal facets, resulting in an orientation change and the assembly of the following growth. Thus, the crystal grows in the planes of preference, and the frequent morphologies from the green-synthesized nanomaterials are wires, cubes, hexagons, pentagons, rods, spheres and triangles [41–46]. In the synthesis of CuO-ZnO NCs, there is no conclusion drawn for the formation of NCs. After the formation of metal oxides synthesized through the aforementioned mechanisms, it is hypothesized that coordinate covalent bonds are formed in between CuO and ZnO, using the lone-pair electron from their own oxygen atom to bond the metal oxides together in forming CuO-ZnO NCs [38]. The proposed mechanism is shown in Figure 8.

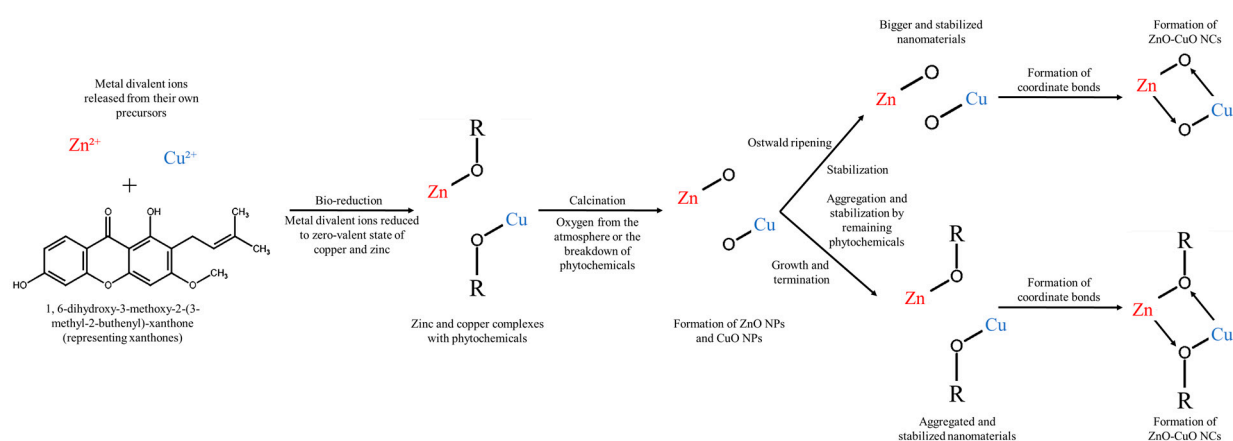


Figure 8. Hypothesized mechanisms in green-synthesizing nanomaterials using mangosteen-leaf aqueous extract via bio-reduction. R represents 1, 6-dihydroxy-3-methoxy-2-(3-methyl-2-butenyl)-xanthone (the xanthone found in mangosteen leaves), demonstrating the hypothesized mechanisms in green-synthesizing nanomaterials. The Cu^{2+} and Zn^{2+} were released upon precursors being added to the mangosteen-leaf aqueous extract. During the calcination process, the metal oxide nanomaterials are formed instantly by reacting with oxygen from atmosphere or the breakdown of phytochemicals. Subsequently, the metal oxide nanomaterials are also aggregated and stabilized by the presence of the remaining phytochemicals in the bio-reduction mechanism. Also, the metal oxide nanomaterials are stabilized and became bigger, due to the occurrence of Ostwald ripening. For the formation of CuO-ZnO NCs, the coordinate covalent bonds are further formed using the oxygen atom lone pairs in the nano-sized CuO and ZnO to bond with each other, resulting in NCs.

The XRD patterns were well-defined, intense and narrow diffraction peaks, which demonstrated the good crystalline nature of the synthesized nanomaterials [21,32,47–49] due to the removal of organic materials during calcination, boosting their crystallinities [50]. The strong intensities at the (0 0 2) and (1 1 1) peaks showed that they were preferential crystal planes of synthesized CuO NPs [51]. Similarly, the synthesized ZnO NPs were preferential crystal planes at (1 0 0), (0 0 2) and (1 0 1) peaks, as those intensities of peaks were

stronger than other peaks [52]. In particular, the strong intensity of (0 0 2) suggested the synthesized ZnO NPs was grown along the *c*-axis [15]. The detection of monoclinic-tenorite and hexagonal-zincite phases in the CuO-ZnO NCs indicated the successful synthesizing of the heterojunction semiconductor [20]. The CuO-indexed peaks were higher than in ZnO, indicating the contribution of copper in the formation of heterojunction nanomaterial [26,53,54] and reflecting its high weight percentage in synthesizing CuO-ZnO NCs [55,56]. The larger crystalline size in CuO-ZnO NCs, compared to the pure metal oxide nanomaterials, might be due to the cooperation of ZnO and CuO during the synthesis, resulted in the forming of a greater crystalline size than in pure nanomaterials. This shown that the crystalline size of heterojunction nanomaterial was affected by the addition of a precursor [36]. Moreover, the strain resulting from non-uniform lattice distortion and crystal-phase dislocation widened and caused a slight shifting of the peaks in the synthesized CuO-ZnO NCs because of the rearrangement of CuO and ZnO crystalline phases in the heterojunction nanomaterial [15,54,57]. As a result, the great number of interfaces in each volume led to a small crystalline size [58], with the increase in micro-strain level [57]. The unidentified peaks in the XRD patterns were contributed to by the impurities due to the soot remaining after the burning of attached phytochemicals on the synthesized nanomaterials' surface during the calcination process [58].

The great difference between XRD and FE-SEM measurements was due to FE-SEM providing visualization of shape and morphology, while XRD offers a measurement of the nanomaterial's crystalline region diffracted coherently by X-ray [15]. The high viscosity of plant extract [49], surface physicochemical characteristics [48,59–61], strong force of attraction [33,62], metal oxide nanomaterial oxidation [63] and the occurrence of isotropic aggregation at the isoelectric point [15,61], kept the synthesized nanomaterials firmly bound together to form a nanostructure that was almost spherical [36]. The green-synthesized nanomaterial aggregation was potentially caused by the nucleation of copper and zinc ions during the reduction of salt precursors by the phytochemicals from the mangosteen-leaf aqueous extract [37]. This proved the capping and reducing properties and the ability of phytochemicals during the green synthesis of CuO NPs, ZnO NPs and CuO-ZnO NCs. Additionally, the aggregation of synthesized nanomaterials might be caused by the excess hydrogen cations from the moisture surface of the nanomaterials. The monodispersed and smoother surface was observed for CuO NPs and ZnO NPs, due to the fact that only the single phase was synthesized in pure NPs [64]. The formation of a porous structure in ZnO NPs could be caused by gas escaping at high temperature during the calcination process [65]. A similar observation also occurred in the green synthesizing of ZnO NPs by using *Ocimum gratissimum* leaf extract [66].

The appearance of carbon weak signal was due to the application of carbon tape for attaching the synthesized nanomaterials during the analysis [15] and the leftover soot, the impurities caused by the burning of organic materials during the calcination [67]. Since it only showed up as a minor element and had minor minimal interaction with the synthesized nanomaterials, this was not a problem [68]. The detection of copper and zinc in heterojunction NCs revealed the incorporation of ZnO within CuO [69] and successfully synthesized NCs in the desired ratio. The presence of an oxygen signal in EDX spectra revealed that the synthesized nanomaterials were in oxidized form [25].

The formation of nanomaterials was confirmed by the cooler changes of the extract [70] of mangosteen leaf. After adding $\text{Cu}(\text{NO}_3)_2 \cdot 3\text{H}_2\text{O}$ and/or $\text{Zn}(\text{NO}_3)_2 \cdot 6\text{H}_2\text{O}$ to mangosteen-leaf aqueous extract, the light-brown plant extract immediately changed to russet, greenish brown and brown, revealing the production of Cu^0 and Zn^0 after the Cu^{2+} and Zn^{2+} reduction by the presence of phytochemicals in the plant extract. Later, the Cu^0 and Zn^0 were oxidized into CuO, ZnO and CuO-ZnO, respectively. The synthesized nanomaterials' absorption peaks were detected by the occurrence of surface plasmon resonance (SPR) phenomena at a specific wavelength [18,22,70] when the incident-light wavelength was larger than the size of the particle. The SPR absorption of nanomaterials was related to the collective oscillation of electromagnetically induced free conduction-band

electrons [18]. Therefore, the differences in crystallinity, crystalline size, morphology and presence of defects explained the absorption behavior of the synthesized nanomaterials [15]. A bathochromic shift in UV-Vis spectra was observed, indicating a reduction in the CuO-ZnO NCs energy bandgap, resulting from the simplified electron transition in heterojunction NCs when compared with CuO NPs and ZnO NPs [58].

The synthesized nanomaterials' energy bandgaps were best fitted with direct transition, as they have an occupied d -shell in respective cations and high electronegativity in the anion [71]. The larger energy bandgap in synthesized CuO NPs compared to their bulk is due to the occurrence of the quantum confinement effect when the crystalline size is smaller than excited e^-/h^+ pair Bohr radius, resulting in an energy bandgap increase when particle size decreases [15]. The ZnO NPs energy bandgap was smaller than that of CuO NPs, due to its larger oxygen deficiency, higher lattice strain, smaller grain size and rougher surface [32]. The synthesized CuO-ZnO NCs have the lowest energy bandgap, which could be caused by the pure metal oxide nanomaterials having nearer band edges due to the high ionicity between the cation and anion, which causes a high energy bandgap and an increase in the splitting of dangling-bond orbitals. In contrast, in heterojunction NCs, the additional of impurities resulted in secondary bonding–antibonding interaction and the removal of dangling bonds, giving rise to the extra interactions with occupied or unoccupied orbitals [72]. The electrons transferred from the occupied valence band to the defects' energy level rather than from the transition of the electron from the occupied valence band to the empty conduction band [15]. Additionally, it was widely known that the splitting of each level to sub-levels equal to the number of interacting atoms could cause band overlap in hetero-structured NCs. Therefore, in accordance with the energy bandgap theory, the NCs' energy bandgap ought to rise or fall [73]. Consequently, low-energy states and low ionization energies in synthesized CuO-ZnO NCs are caused by strong interfaces between CuO and ZnO. The interactions between band electrons in the NCs and electrons in the localized d -orbital of copper ions, which replace the zinc ions, could potentially be another reason for the significantly small energy bandgap in synthesized CuO-ZnO NCs [37]. This makes the synthesized CuO-ZnO NCs with the narrowest energy bandgap able to absorb visible light [14], and this works well for photocatalytic applications, as the electrons can be transferred easily from the valance band to the conduction band [15,21,26,32].

The highest COD removal efficiency was recorded using CuO-ZnO NCs under monochromatic blue LED, and could be explained by the attribution of the narrow energy bandgap and existence of oxygen vacancies found in heterojunction NCs. The combination of a wide energy bandgap of CuO in synthesized CuO-ZnO NCs prevented the recombination of the e^-/h^+ pair. Thus, the p -CuO and n -ZnO in the heterojunction NCs improved the e^-/h^+ pair separation by charge-transfer mechanism and intercalation, resulting in improved organic pollutant degradation [14,15,18,19,21] in POME under monochromatic blue LED irradiation. Additionally, the packed structure in synthesized CuO-ZnO NCs sped up the electron flow between the surface and prevented the recombination with holes [14,18]. Generally, to create most white-light diodes, an LED that emits light at a short wavelength is combined with a wavelength converter to create a longer-wavelength secondary emission [74]. As a result, the monochromatic blue LED provided higher photon energy than the polychromatic white LED. On the other hand, there was similar COD removal efficiency of synthesized CuO NPs and ZnO NPs under monochromatic-blue and polychromatic-white LEDs, due to the fact that the direct bandgap semiconductors have better in e^-/h^+ pair separation and recombination, compared to indirect materials [15]. Moreover, the magnetic stirring during the photo-degradation might have contributed to removing the organic pollutant [19].

The band alignment in heterojunctions influences the photocatalytic activity. The bottom conduction-band energy (E_{CB}) and top valance-band energy (E_{VB}) of synthesized CuO-ZnO NCs against the normal hydrogen electrode (NHE) is shown in Figure 9. The conduction- and valance-band locations of CuO NPs was -0.32 and 2.96 eV, while that for ZnO NPs was 0.03 and 2.55 eV. Considering the redox potential of hydroxyl radicals

(HO•, 2.59 eV) and superoxide radicals ($O_2^-•$, -0.16 eV) [21], it could be concluded that the generation of radicals was thermodynamically favored toward CuO NPs as its E_{CB} , and that E_{VB} met the energy requirements, and vice versa for ZnO NPs. The inner electric field at the CuO NP and ZnO NP interface is the reason for the charge separation and transferring [14,15,19]. As for exposing synthesized CuO-ZnO NCs under LEDs, the electrons in the conduction band (e_{CB}^-) of CuO NPs with high energy migrated to the ZnO NP conduction band. The electrons reacted with the absorbed oxygen to form $O_2^-•$. The generation of oxygen vacancies played a role in trapping electrons and active sites, to enhance photocatalytic activity by improving e^-/h^+ pair separation. Likewise, the formation of holes at the valence band (h_{VB}^+) of CuO NPs migrated to the ZnO NPs valence band and reacted with water to produce HO•. Eventually, the highly reactive HO• and $O_2^-•$ radicals degraded the organic components in the POME into carbon dioxide and water. The oxidation and reduction process occurred at the ZnO NP conduction and valence bands in synthesized CuO-ZnO NCs in the Nguyen et al. study, as their ZnO NPs were more thermodynamically favorable for radical generation [21]. The details of proposed mechanisms for the degradation of POME using CuO-ZnO NCs are outlined in Equations (1)–(11) and depicted in Figure 9.

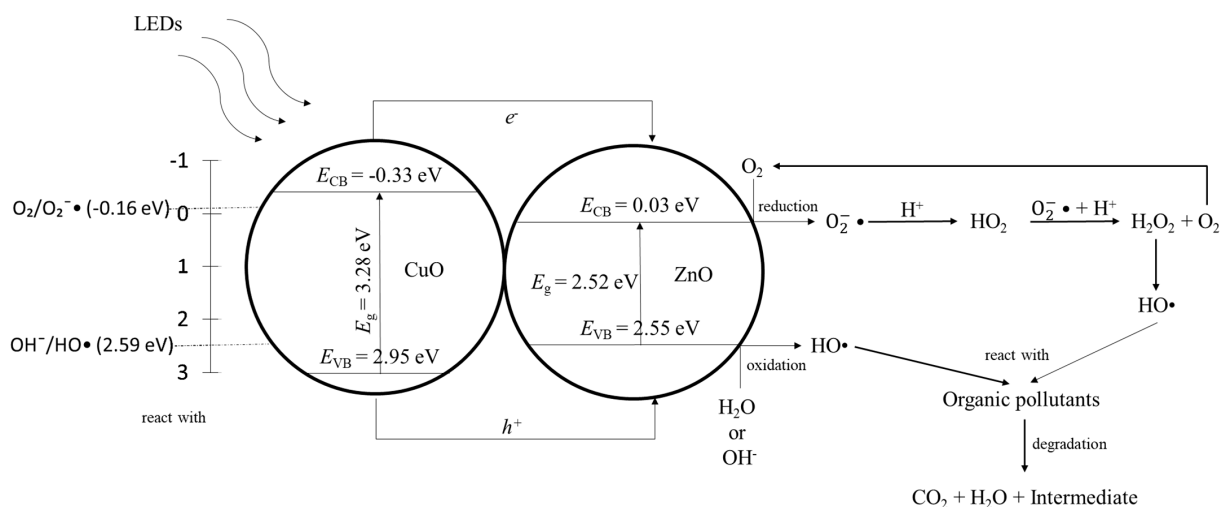
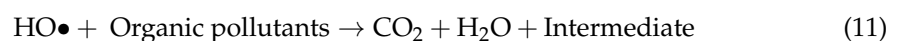
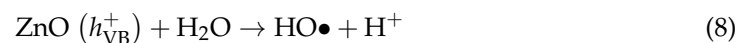
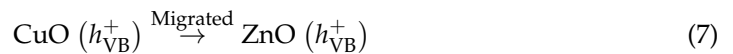
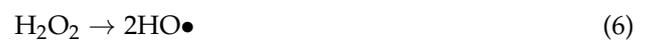
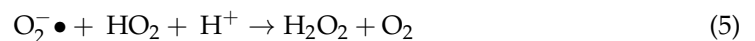
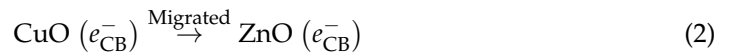
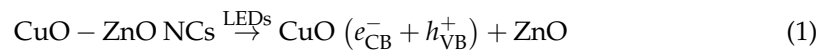


Figure 9. Proposed photodegradation mechanism of CuO-ZnO NCs. Under exposure to LEDs, the e^- and h^+ migrated to ZnO, due to the fact that CuO was thermodynamically favored in generating

reactive radicals ($\text{HO}\bullet$ and $\text{O}_2^-\bullet$ radicals). In ZnO, the oxygen was reduced at the conduction band, while the water or hydroxyl ions were oxidized at the valence band, to produce $\text{HO}\bullet$ radicals. The organic pollutants in the POME reacted with the produced $\text{HO}\bullet$ radicals and eventually degraded these into harmless products, such as carbon dioxide, water and intermediate products. The bottom conduction-band energy, top valence-band energy and the energy bandgap of the synthesized CuO-ZnO NCs are represented by E_{CB} , E_{VB} and E_{g} , respectively, in the figure.

The table below shows the effectiveness in reducing COD from POME in various studies using different nanomaterials (Table 4).

Table 4. Comparison of COD removal efficiency from POME, under different photodegradation conditions, with other studies.

Nanomaterials	Conditions			COD Removal Efficiency (%)	References	
	Light Sources	Nanomaterial Loadings (g/L)	POME Volume (mL)			
CuO	UV light	0.50	300	180	66.00	[48]
TiO ₂	UV light	5.00	250	240	43.00	[75]
TiO ₂	Sunlight	0.02	150	300	54.30	[76]
ZnO	Sunlight	0.20	150	300	40.00	[76]
ZnO	UV light	1.00	400	240	82.00	[77]
ZnO	UV light	1.00	400	120	96.00	[78]
CuO-ZnO	Blue LED	0.75	200	150	63.27	Current study

4. Materials and Methods

The mangosteen leaves were gathered from the Kampar neighborhoods, Malaysia. Without further purification, copper(II) nitrate trihydrate [$\text{Cu}(\text{NO}_3)_2 \cdot 3\text{H}_2\text{O}$] and zinc(II) nitrate hexahydrate [$\text{Zn}(\text{NO}_3)_2 \cdot 6\text{H}_2\text{O}$] were utilized after being acquired from HmbG (Hamburg, Germany) and HiMedia Laboratories Pvt. Ltd. (Nashik, India), respectively. The POME sample was obtained from Selangor and was kept in an airtight container to prevent deterioration during shipping. The low-range COD (LR-COD, 3.00–150.00 mg/L) digestion vials were bought from HACH (Bangkok, Thailand) for COD analysis.

4.1. Preparation of Mangosteen-Leaf Aqueous Extract

Mangosteen (*Garcinia mangostana*)-leaf aqueous extract preparation was adapted from Chan et al.'s work [58]. The leaves were thoroughly rinsed with tap water to eliminate the dust and dried in an oven for two days before being put into a vacuum oven for another eight hours. The dried leaves were ground through a grinder to obtain a fine powder. After that, 3.0 g of powder was added with, 100 mL of deionized water, and heated with stirring for 20 min at 70–80 °C to create 0.03 g/mL of leaf aqueous extract. The leaf aqueous extract was vacuum-filtered and the reddish-brown filtrate was obtained for CuO NPs, ZnO NPs and CuO-ZnO NCs synthesis.

4.2. Synthesis of CuO NPs, ZnO NPs and CuO-ZnO NCs

The green synthesis of CuO NPs, ZnO NPs, and CuO-ZnO NCs was adapted from the methods described by Chan et al. [38,58,79]. Initially, a 30 mL 0.03 g/mL aqueous extract of mangosteen leaf was heated and stirred at 70–80 °C. Subsequently, 2.0 g of $\text{Cu}(\text{NO}_3)_2 \cdot 3\text{H}_2\text{O}$ was added, and the heating and stirring at 70–80 °C were continued until a dark-brown paste was formed. The dark-brown paste was transferred to a ceramic crucible and calcined at 600 °C for 2 h in a muffle furnace to obtain the black CuO powder.

The ZnO NPs and CuO-ZnO NCs were synthesized using the above-mentioned method. The ZnO NPs were synthesized using 1.5 g of $\text{Zn}(\text{NO}_3)_2 \cdot 6\text{H}_2\text{O}$, and a fine white powder was obtained. Meanwhile, 2.0 g of $\text{Cu}(\text{NO}_3)_2 \cdot 3\text{H}_2\text{O}$ and 1.5 g of $\text{Zn}(\text{NO}_3)_2 \cdot 6\text{H}_2\text{O}$ were used in synthesizing the dark-brown CuO-ZnO NCs powder.

4.3. Characterization of CuO NPs, ZnO NPs and CuO-ZnO NCs

The Fourier-transform infrared spectroscopy (FT-IR, Perkin Elmer RX1 spectrophotometer, Waltham, MA, USA) study was carried out at room temperature in the range of 4000–400 cm^{-1} with resolution of 4 cm^{-1} , by using potassium bromide pellets. The calculated $\nu(\text{M-O})$ band of synthesized nanomaterials using Hooke's Law expression [34] is shown in Equation (12).

$$\nu = 4.12 \sqrt{\frac{K}{\mu}} \quad (12)$$

where

ν = Frequency (cm^{-1});

K = Force constant (5×10^5 dynes/cm);

μ = Masses of atoms (g).

X-ray powder diffraction (XRD) patterns were obtained by an X-ray diffractometer (Shimadzu XRD 6000, Kyoto, Japan) operating in continuous scanning mode at 40 kV/30 mA and for 0.02 min^{-1} with Cu $K\alpha$ radiation ($\lambda = 1.5406 \text{ \AA}$) in the 2θ range from 10 to 80°. By using the XRD data obtained, the synthesized nanomaterials' average crystalline size, dislocation density and micro strain was calculated based on the Debye-Scherrer's, Williamson-Smallman's and micro-strain relation formulae [38,54] below, respectively.

$$D = \frac{0.94\lambda}{\beta \cos \theta} \quad (13)$$

$$\delta = \frac{1}{D^2} \quad (14)$$

$$\varepsilon = \frac{\beta \cos \theta}{4} \quad (15)$$

where

D = Crystalline size (nm);

δ = Dislocation density ($\times 10^{14} \text{ cm}^{-1}$);

ε = Micro strain ($\times 10^{-4}$);

λ = Wavelength of X-ray;

β = Full width at half maximum (FWHM) of peak;

θ = Bragg angle.

A field-emission scanning electron microscope (FE-SEM, JEOL JSM-6710F, Kyoto, Japan) with an energy-dispersive X-ray (EDX) analyzer (X-max, 150 Oxford Instruments, Oxford, UK) was used to examine the morphology and elemental composition of CuO NPs, ZnO NPs and CuO-ZnO NCs. A high-resolution transmission electron microscope (HR-TEM, JEOL JEM-2100F, Nagoya-shi, Japan) at 200 kV was applied for viewing in depth the CuO-ZnO NCs morphology. A Thermo Scientific (Waltham, MA, USA) GENESYS 10S UV-Vis spectrophotometer was used to detect the CuO NPs, ZnO NPs and CuO-ZnO NCs absorption spectra. The energy bandgap of the synthesized nanomaterials was plotted and best-fitted, using $(\alpha hv)^n$ versus hv from the Tauc approach [20], as in Equation (16).

$$\alpha hv = A(hv - E_g)^n \quad (16)$$

where

α = Absorption coefficient;

A = Constant;

E_g = Energy bandgap (eV);

h = Planck's constant (6.626×10^{-34} Js);

n = Exponential factor of electronic transition;

($n = \frac{1}{2}$, for indirect transition; $n = 2$, for direct transition).

The positions of the bottom conduction-band energy and top valence-band energy were predicted against the NHE, based on the Mulliken electronegativity theory [20,21], in Equations (17) and (18), respectively.

$$E_{CB} = \chi - E_e - 0.5E_g \quad (17)$$

$$E_{VB} = \chi - E_e + 0.5E_g \quad (18)$$

where

E_{CB} = Bottom conduction-band energy (eV);

E_{VB} = Top valence-band energy (eV);

χ = Absolute electronegativity of semiconductor (CuO = 5.81, ZnO = 5.79);

E_e = Free electron energy in the hydrogen scale (4.50 eV).

4.4. Photocatalytic Performance

The photocatalytic performance of green-synthesized nanomaterials was determined by the COD removal efficiency in the POME treatment, with slight modification, based on the study by Phang et al. [48]. The 200 mL of POME was diluted with distilled water to achieve a COD value in the range of 200.00–210.00 mg/L, ensuring adequate light penetration for degradation. The diluted POME was stirred in the dark for 50 min to achieve adsorption–desorption equilibrium between the POME and 150 mg of nanomaterials. Then, the suspension was exposed to blue and white LEDs (4 W in power and voltage in 220 V and 50 Hz), respectively, for 2.5 h. Next, 2 mL of untreated and treated POME were withdrawn for COD value determination. The withdrawn solutions were added to LR-COD vials and digested at 150 °C for 2 h using a HACH DRB 200 COD digital reactor (HACH Company, Berlin, Germany). The COD values were then measured using a DR3900 digital reactor without RFID (HACH Company, Germany) with program 430. The COD removal efficiency (in percentage) for CuO NPs, ZnO NPs, and CuO-ZnO NCs was determined using Equation (19).

$$\text{COD removal (\%)} = \frac{\text{COD}_i - \text{COD}_f}{\text{COD}_f} \times 100\% \quad (19)$$

where

i = Initial value of COD in mg/L;

f = Final value of COD after photo-degradation in mg/L.

4.5. Statistical Analysis

The removal efficiency of COD (in percentage) by synthesized CuO NPs, ZnO NPs and CuO-ZnO NCs were presented as mean \pm standard deviation (SD). A two-way ANOVA analysis and Tukey's test were performed to compare the COD removal efficiency by different synthesized nanomaterials from mangosteen-leaf aqueous extract and mono- and polychromatic visible lights, respectively, using Microsoft Excel 2013, by setting p -value < 0.05 as a significant criterion.

5. Conclusions

This study has demonstrated the green synthesis of CuO NPs, ZnO NP, and CuO-ZnO nanomaterials utilizing mangosteen-leaf aqueous extract. Among the synthesized nanomaterials, the CuO-ZnO NCs, with an average crystalline size of 29.04 nm and particle size of 82.32 nm, exhibited a spherical shape and the lowest energy bandgap of 1.61 eV. These attributes contributed to their superior performance in COD removal from POME, particularly under blue LED irradiation. The application of CuO-ZnO NCs resulted in a COD removal efficiency of $63.27\% \pm 0.010$, reducing the COD value to $75.67 \text{ mg/L} \pm 2.517$, which is notably below the discharge limit mandated by the Department of Environment in Malaysia (100.00 mg/L). Under white-LED irradiation, the COD removal efficiency was observed at $35.77\% \pm 0.017$. Through the lens of environmental sustainability and

technological innovation, this research highlights the effectiveness of green-synthesized heterojunction materials as a viable photocatalyst. They not only significantly reduce the COD in POME to meet regulatory standards, but they also offer a cost-effective and environmentally friendly solution to a pressing industrial challenge. Future work should aim to optimize these photocatalytic processes and explore the scalability of this green-synthesis approach for broader environmental applications.

Author Contributions: Conceptualization, M.A. (Mohammad Aminuzzaman) and L.-H.T.; methodology, M.A. (Mohammad Aminuzzaman); formal analysis, S.K.G., Y.B.C., S.D. and H.A.; resources, Y.B.C. and M.A. (Mohammad Aminuzzaman); writing—original draft preparation, Y.B.C., M.A. (Mohammad Aminuzzaman), L.-H.T. and Y.F.W.; writing—review and editing, M.A. (Mohammad Aminuzzaman), L.-H.T., Y.F.W. and M.A. (Md. Akhtaruzzaman); supervision, M.A. (Mohammad Aminuzzaman) and L.-H.T.; project administration, M.A. (Mohammad Aminuzzaman) and L.-H.T.; funding acquisition, M.A. (Mohammad Aminuzzaman), L.-H.T., L.S.W. and M.A. (Md. Akhtaruzzaman). All authors have read and agreed to the published version of the manuscript.

Funding: This research was funded by University Tunku Abdul Rahman, grant number UTARRF (IPSR/RMC/UTARRF/202-C2/M01) and Research, Development and Innovative Authority (RDIA) of the Kingdom of Saudi Arabia, grant number (12615-iu-2023-IU-R-2-1-EI-).

Data Availability Statement: The data presented in this study are available upon request from the corresponding author.

Acknowledgments: The authors would like to express their appreciation to University Tunku Abdul Rahman (UTAR) for providing financial support through UTARRF (IPSR/RMC/UTARRF/202-C2/M01) and research facilities to carry out the research work. The authors also wish to extend their sincere gratitude to the Deanship of Graduate Studies and Scientific Research at the Islamic University of Madinah for the support provided to the research support program. Moreover, the authors would also like to thank University Malaya (UM) for providing HR-TEM service and analysis.

Conflicts of Interest: The authors declare no conflicts of interest.

References

1. Igwe, J.C.; Onyegbado, C.C. A Review of palm oil mill effluent (POME) water treatment. *Glob. J. Env. Res.* **2007**, *1*, 54–62.
2. Mahmod, S.S.; Takriff, M.S.; AL-Rajabi, M.M.; Abdul, P.M.; Gunny, A.A.N.; Silvamany, H.; Jahim, J.M. Water reclamation from palm oil mill effluent (POME): Recent technologies, by-product recovery, and challenges. *J. Water. Process. Eng.* **2023**, *52*, 103488–103502. [[CrossRef](#)]
3. Sidik, D.A.B.; Hairom, N.H.H.; Rozman, A.I.; Johari, M.J.S.; Muhammad, A. The photocatalytic activity of green zinc oxide nanoparticles in the treatment of aerobically palm oil mill effluent. *J. Sci. Technol.* **2023**, *15*, 7–15. [[CrossRef](#)]
4. Agustina, L.; Suprihatin, S.; Romli, M.; Suryadarma, P. Processing of palm mill oil effluent using photocatalytic: A literature review. *J. Ecol. Eng.* **2021**, *22*, 43–52. [[CrossRef](#)] [[PubMed](#)]
5. Mahmod, S.S.; Arisht, S.N.; Jahim, J.M.; Takriff, M.S.; Tan, J.P.; Luthfi, A.A.I.; Abdul, P.M. Enhancement of biohydrogen production from palm oil mill effluent (POME): A review. *Int. J. Hydrogen Energy* **2021**, *47*, 40637–40655. [[CrossRef](#)]
6. Puasa, N.A.; Hairom, N.H.H.; Dzinun, H.; Madon, R.H.; Ahmad, N.S.; Sidik, D.A.B.; Azmi, A.A.A.R. Photocatalytic degradation of palm oil mill secondary effluent in presence of zinc oxide nanoparticles. *Environ. Nanotechnol. Monit. Manag.* **2021**, *15*, 100413–100418. [[CrossRef](#)]
7. Ratnasari, A.; Zaidi, N.S.; Syafiuddin, A.; Boopathy, R.; Kueh, A.B.H.; Amalia, R.; Prasetyo, D.D. Prospective biodegradation of organic and nitrogenous pollutants from palm oil mill effluent by acidophilic bacteria and archaea. *Bioresour. Technol. Rep.* **2021**, *15*, 100809–100819. [[CrossRef](#)]
8. Saputera, W.H.; Amri, A.F.; Mukti, R.R.; Suendo, V.; Devianto, H.; Sasongko, D. Photocatalytic degradation of palm oil mill effluent (POME) waste using BiVO₄ based catalysts. *Molecules* **2021**, *26*, 6225. [[CrossRef](#)] [[PubMed](#)]
9. Saputera, W.H.; Amri, A.F.; Daiyan, R.; Sasongko, D. Photocatalytic technology for palm oil mill effluent (POME) wastewater treatment: Current progress and future perspective. *Materials* **2021**, *14*, 2846. [[CrossRef](#)]
10. Obayomi, K.S.; Lau, S.Y.; Danquah, M.K.; Zhang, J.; Chiong, T.; Takeo, M.; Jeevanandam, J. Novel concepts for graphene-based nanomaterials synthesis for phenol removal from palm oil mill effluent (POME). *Materials* **2023**, *16*, 4379. [[CrossRef](#)]
11. Aqilah Mohd Razali, N.; Norharyati Wan Salleh, W.; Rosman, N.; Hafiza Ismail, N.; Zu Nurain Ahmad, S.; Aziz, F.; Jye, L.W.; Fauzi Ismail, A. Palm oil mill effluent treatment using tungsten trioxide: Adsorption and photocatalytic degradation. *Mater. Today Proc.* **2020**, *42*, 22–27. [[CrossRef](#)]
12. Osman, N.A.; Ujang, F.A.; Roslan, A.M.; Ibrahim, M.F.; Hassan, M.A. The effect of palm oil mill effluent final discharge on the characteristics of *Pennisetum purpureum*. *Sci. Rep.* **2020**, *10*, 6613–6622. [[CrossRef](#)] [[PubMed](#)]

13. Septiningrum, F.; Yuwono, A.H.; Maulana, F.A.; Nurhidayah, E.; Dhaneaswara, D.; Sofyan, N.; Hermansyah, H.; Purwanto, W.W. Mangosteen pericarp extract mediated synthesis of Ag/TiO₂ nanocomposite and its application on organic pollutant degradation by adsorption-photocatalytic activity. *Curr. Res. Green. Sustain. Chem.* **2024**, *8*, 100394–100404. [[CrossRef](#)]
14. Dien, N.D.; Ha, P.T.T.; Vu, X.H.; Trang, T.T.; Giang, T.D.T.; Dung, N.T. Developing efficient CuO nanoplate/ZnO nanoparticle hybrid photocatalysts for methylene blue degradation under visible light. *R. Soc. Chem. Adv.* **2023**, *13*, 24505–24518. [[CrossRef](#)] [[PubMed](#)]
15. Mrabet, C.; Jaballah, R.; Mahdhi, N.; Boukhachem, A.; Amlouk, M. CuO-ZnO nanocomposites-based thin films: Characterization, physical properties and sunlight photocatalytic degradation of organic pollutants. *J. Alloys Compd.* **2023**, *968*, 172252–172266. [[CrossRef](#)]
16. Cheng, Y.W.; Chong, C.C.; Lam, M.K.; Ayoub, M.; Cheng, C.K.; Lim, J.W.; Yusup, S.; Tang, Y.; Bai, J. Holistic process evaluation of non-conventional palm oil mill effluent (POME) treatment technologies: A conceptual and comparative review. *J. Hazard. Mater.* **2021**, *409*, 124964–124996. [[CrossRef](#)] [[PubMed](#)]
17. Bandekar, S.S.; Hosamane, S.N.; Patil, C.; Yaragatti, A.; Hukerikar, A.; Patil, S.; Chachadi, P. ZnO-CuO nanocomposites: Synthesis, characterization and antibacterial activity. *J. Phys. Conf. Ser.* **2020**, *1706*, 012018–012023. [[CrossRef](#)]
18. Basit, R.A.; Abbasi, Z.; Hafeez, M.; Ahmad, P.; Khan, J.; Khandaker, M.U.; Al-Mugren, K.S.; Khalid, A. Successive photocatalytic degradation of methylene blue by ZnO, CuO and ZnO/CuO synthesized from *Coriandrum sativum* plant extract via green synthesis technique. *Crystals* **2023**, *13*, 281. [[CrossRef](#)]
19. Li, H.; Ma, W.; Zeng, X.; Liu, S.; Xiao, L.; Fang, Z.; Feng, Y.; Yang, M.; Zhu, H.; Yang, Y.; et al. ZnO/CuO Piezoelectric nanocatalysts for the degradation of organic pollutants. *ACS. Appl. Nano. Mater.* **2023**, *6*, 21113–21122. [[CrossRef](#)]
20. Mubeen, K.; Irshad, A.; Safeen, A.; Aziz, U.; Safeen, K.; Ghani, T.; Khan, K.; Ali, Z.; ul Haq, I.; Shah, A. Band structure tuning of ZnO/CuO composites for enhanced photocatalytic activity. *J. Saudi. Chem. Soc.* **2023**, *27*, 101639–101651. [[CrossRef](#)]
21. Nguyen, T.T.T.; Nguyen, Y.N.N.; Tran, X.T.; Nguyen, T.T.T.; Tran, T.V. Green synthesis of CuO, ZnO and CuO/ZnO nanoparticles using *Annona glabra* leaf extract for antioxidant, antibacterial and photocatalytic activities. *J. Environ. Chem. Eng.* **2023**, *11*, 111003–111016. [[CrossRef](#)]
22. Takele, E.; Bogale, R.F.; Shumi, G.; Kenasa, G. Green synthesis, characterization, and antibacterial activity of CuO/ZnO nanocomposite using *Zingiber officinale* rhizome extract. *J. Chem.* **2023**, *2023*, 20233481389. [[CrossRef](#)]
23. Vindhya, P.S.; Kavitha, V.T. Effect of cobalt doping on antimicrobial, antioxidant and photocatalytic activities of CuO nanoparticles. *Mater. Sci. Eng. B.* **2023**, *289*, 116258–116270. [[CrossRef](#)]
24. Zelekew, O.A.; Haitosa, H.H.; Chen, X.; Wu, Y.-N. Recent progress on plant extract-mediated biosynthesis of ZnO-based nanocatalysts for environmental remediation: Challenges and future outlooks. *Adv. Colloid. Interface Sci.* **2023**, *317*, 102931–102951. [[CrossRef](#)] [[PubMed](#)]
25. Adeyemi, J.O.; Onwudiwe, D.C.; Oyediji, A.O. biogenic synthesis of CuO, ZnO, and CuO–ZnO nanoparticles using leaf extracts of *Dovyalis caffra* and their biological properties. *Molecules* **2022**, *27*, 3206. [[CrossRef](#)]
26. Bekru, A.G.; Tufa, L.T.; Zelekew, O.A.; Goddati, M.; Lee, J.; Sabir, F.K. Green synthesis of a CuO–ZnO nanocomposite for efficient photodegradation of methylene blue and reduction of 4-nitrophenol. *ACS Omega* **2022**, *7*, 30908–30919. [[CrossRef](#)] [[PubMed](#)]
27. Zainal, N.H.; Jalani, N.F.; Mamat, R.; Astimar, A.A. A review on the development of palm oil mill effluent (POME) final discharge polishing treatments. *J. Oil Palm Res.* **2017**, *29*, 528–540. [[CrossRef](#)]
28. Andani, R.; Fajrina, A.; Asra, R.; Eriadi, A. Antibacterial activity test of mangosteen plants (*Garcinia mangostana* L.): A review. *Asian J. Pharm. Res. Dev.* **2021**, *9*, 164–171. [[CrossRef](#)]
29. Diniatik, D.; Anggraeni, R.S. Antibacterial (*Staphylococcus aureus* and *Escherichia coli*) and antifungal (*Saccharomyces cerevisiae*) activity assay on nanoemulsion formulation of ethanol extract of mangosteen leaves (*Garcinia mangostana* L.) as fruit preservative. *J. Food Pharm. Sci.* **2021**, *9*, 351–365. [[CrossRef](#)]
30. Jassim, A.M.N.; Shafy, G.M.; Mohammed, M.T.; Farhan, S.A.; Noori, O.M. Antioxidant, anti-inflammatory and wound healing of biosynthetic gold nanoparticles using mangosteen (*G. mangostana*). *Iraqi J. Ind. Res.* **2021**, *8*, 59–74. [[CrossRef](#)]
31. Tran, V.A.; Vo, T.-T.T.; Nguyen, M.-N.T.; Dat, N.D.; Doan, V.-D.; Nguyen, T.-Q.; Vu, Q.H.; Le, V.T.; Tong, T.D. Novel α -mangostin derivatives from mangosteen (*Garcinia mangostana* L.) peel extract with antioxidant and anticancer potential. *J. Chem.* **2021**, *2021*, 9985604. [[CrossRef](#)]
32. Jaithon, T.; Atichakaro, T.; Phonphoem, W.; T-Thienprasert, J.; Sreewongchai, T.; T-Thienprasert, N.P. Potential usage of biosynthesized zinc oxide nanoparticles from mangosteen peel ethanol extract to inhibit *Xanthomonas oryzae* and promote rice growth. *Heliyon* **2024**, *10*, e24076–e24085. [[CrossRef](#)] [[PubMed](#)]
33. Yusefi, M.; Shameli, K.; Yee, O.S.; Teow, S.Y.; Hedayatnasab, Z.; Jahangirian, H.; Webster, T.J.; Kuča, K. Green synthesis of Fe₃O₄ nanoparticles stabilized by a *Garcinia mangostana* fruit peel extract for hyperthermia and anticancer activities. *Int. J. Nanomed.* **2021**, *16*, 2515–2532. [[CrossRef](#)] [[PubMed](#)]
34. Pavia, D.L.; Lampman, G.M.; Kriz, G.S.; Vyvyan, J.R. *Introduction to Spectrometry*, 5th ed.; Nelson Education Ltd.: Stamford, CT, USA, 2015; pp. 1–690.
35. Suresh, S.; Gunasekaran, S.; Srinivasan, S. Vibrational spectra (FT-IR, FT-Raman), frontier molecular orbital, first hyperpolarizability, NBO analysis and thermodynamics properties of Piroxicam by HF and DFT methods. *Spectrochim. Acta Part A Mol. Biomol. Spectrosc.* **2015**, *138*, 447–459. [[CrossRef](#)]

36. Kaningini, A.G.; Azizi, S.; Sintwa, N.; Mokallane, K.; Mohale, K.C.; Mudau, F.N.; Maaza, M. Effect of optimized precursor concentration, temperature, and doping on optical properties of ZnO nanoparticles synthesized via a green route using bush tea (*Athrixia phylicoides* DC.) leaf extracts. *ACS Omega* **2022**, *7*, 31658–31666. [[CrossRef](#)]
37. Khan, M.I.; Fatima, N.; Shakil, M.; Tahir, M.B.; Riaz, K.N.; Rafique, M.; Iqbal, T.; Mahmood, K. Investigation of in vitro antibacterial and seed germination properties of green synthesized pure and nickel doped ZnO nanoparticles. *Phys. B Phys. Condens. Matter* **2021**, *601*, 412563. [[CrossRef](#)]
38. Chan, Y.B.; Aminuzzaman, M.; Tey, L.-H.; Win, Y.F.; Watanabe, A.; Djearamame, S.; Akhtaruzzaman, M. Impact of diverse parameters on the physicochemical characteristics of green-synthesized zinc oxide–copper oxide nanocomposites derived from an aqueous extract of *Garcinia mangostana* L. leaf. *Materials* **2023**, *16*, 5421. [[CrossRef](#)]
39. Selvanathan, V.; Aminuzzaman, M.; Tan, L.X.; Yip, F.W.; Eddy Cheah, S.G.; Heng, M.H.; Tey, L.H.; Arullappan, S.; Algethami, N.; Alharthi, S.S.; et al. Synthesis, characterization, and preliminary in vitro antibacterial evaluation of ZnO nanoparticles derived from soursop (*Annona muricata* L.) leaf extract as a green reducing agent. *J. Mater. Res. Technol.* **2022**, *20*, 2931–2941. [[CrossRef](#)]
40. Parapat, R.Y.; Schwarze, M.; Ibrahim, A.; Tasbihi, M.; Schomäcker, R. Efficient preparation of nanocatalysts. Case study: Green synthesis of supported Pt nanoparticles by using microemulsions and mangosteen peel extract. *R. Soc. Chem. Adv.* **2022**, *12*, 34346–34358. [[CrossRef](#)]
41. Cao, D.; Gong, S.; Shu, X.; Zhu, D.; Liang, S. Preparation of ZnO nanoparticles with high dispersibility based on oriented attachment (OA) process. *Nanoscale. Res. Lett.* **2019**, *14*, 210. [[CrossRef](#)]
42. Fawcett, D.; Verduin, J.J.; Shah, M.; Sharma, S.B.; Poinern, G.E.J. A review of current research into the biogenic synthesis of metal and metal oxide nanoparticles via marine algae and seagrasses. *J. Nanosci.* **2017**, *2017*, 1–15. [[CrossRef](#)]
43. Jeevanandam, J.; Chan, Y.S.; Danquah, M.K. Biosynthesis of metal and metal oxide nanoparticles. *Chem. Bio. Eng. Rev.* **2016**, *3*, 55–67. [[CrossRef](#)]
44. Shah, M.; Fawcett, D.; Sharma, S.; Tripathy, S.K.; Poinern, G.E.J. Green synthesis of metallic nanoparticles via biological entities. *Materials* **2015**, *8*, 7278–7308. [[CrossRef](#)]
45. Singh, J.; Dutta, T.; Kim, K.H.; Rawat, M.; Samddar, P.; Kumar, P. “Green” synthesis of metals and their oxide nanoparticles: Applications for environmental remediation. *J. Nanobiotechnol.* **2018**, *16*, 84. [[CrossRef](#)]
46. Sharma, D.; Kanchi, S.; Bisetty, K. Biogenic synthesis of nanoparticles: A review. *Arab. J. Chem.* **2019**, *12*, 3576–3600. [[CrossRef](#)]
47. Amin, F.; Fozia; Khattak, B.; Alotaibi, A.; Qasim, M.; Ahmad, I.; Ullah, R.; Bourhia, M.; Gul, A.; Zahoor, S.; et al. Green synthesis of copper oxide nanoparticles using *Aerva javanica* leaf extract and their characterization and investigation of in vitro antimicrobial potential and cytotoxic activities. *Evid. Based Complement. Altern. Med.* **2021**, *2021*, 589703. [[CrossRef](#)]
48. Phang, Y.-K.; Aminuzzaman, M.; Akhtaruzzaman, M.; Muhammad, G.; Ogawa, S.; Watanabe, A.; Tey, L.-H. Green synthesis and characterization of CuO nanoparticles derived from papaya peel extract for the photocatalytic degradation of palm oil mill effluent (POME). *Sustainability* **2021**, *13*, 796. [[CrossRef](#)]
49. Siddiqui, V.U.; Ansari, A.; Chauhan, R.; Siddiqi, W.A. Green synthesis of copper oxide (CuO) nanoparticles by *Punica granatum* peel extract. *Mater. Today Proc.* **2021**, *36*, 751–755. [[CrossRef](#)]
50. Park, G.C.; Seo, T.Y.; Park, C.H.; Lim, J.H.; Joo, J. Effects of calcination temperature on morphology, microstructure, and photocatalytic performance of TiO₂ mesocrystals. *Ind. Eng. Chem. Res.* **2017**, *56*, 8235–8240. [[CrossRef](#)]
51. Habibi, M.H.; Karimi, B. Effect of the annealing temperature on crystalline phase of copper oxide nanoparticle by copper acetate precursor and sol-gel method. *J. Therm. Anal. Calorim.* **2014**, *115*, 419–423. [[CrossRef](#)]
52. Yusoff, H.M.; Idris, N.H.; Hipul, N.F.; Yusoff, N.F.M.; Izham, N.Z.M.; Bhat, I.U.H. Green synthesis of zinc oxide nanoparticles using black tea extract and its potential as anode material in sodium-ion batteries. *Malays. J. Chem.* **2020**, *22*, 43–51.
53. Fouda, A.; Salem, S.S.; Wassel, A.R.; Hamza, M.F.; Shaheen, T.I. Optimization of green biosynthesized visible light active CuO/ZnO nano-photocatalysts for the degradation of organic methylene blue dye. *Heliyon* **2020**, *6*, e04896–e04908. [[CrossRef](#)]
54. Hitkari, G.; Chowdhary, P.; Kumar, V.; Singh, S.; Motghare, A. Potential of copper-zinc oxide nanocomposite for photocatalytic degradation of congo red dye. *Clean. Chem. Eng.* **2022**, *1*, 100003–100009. [[CrossRef](#)]
55. Mohammadi-Aloucheh, R.; Habibi-Yangjeh, A.; Bayrami, A.; Latifi-Navid, S.; Asadi, A. Enhanced anti-bacterial activities of ZnO nanoparticles and ZnO/CuO nanocomposites synthesized using *Vaccinium arctostaphylos* L. fruit extract. *Artif. Cells Nanomed. Biotechnol.* **2018**, *46*, 1200–1209. [[CrossRef](#)]
56. Mohammadi-Aloucheh, R.; Habibi-Yangjeh, A.; Bayrami, A.; Latifi-Navid, S.; Asadi, A. Green synthesis of ZnO and ZnO/CuO nanocomposites in *Mentha longifolia* leaf extract: Characterization and their application as anti-bacterial agents. *J. Mater. Sci. Mater. Electron.* **2018**, *29*, 13596–13605. [[CrossRef](#)]
57. Siddiqui, V.U.; Ansari, A.; Ansari, M.T.; Akram, M.K.; Siddiqi, W.A.; Alosaimi, A.M.; Hussein, M.; Rafatullah, M. Optimization of facile synthesized ZnO/CuO nanophotocatalyst for organic dye degradation by visible light irradiation using response surface methodology. *Catalysts* **2021**, *11*, 1509. [[CrossRef](#)]
58. Chan, Y.B.; Selvanathan, V.; Tey, L.-H.; Akhtaruzzaman, M.; Anur, F.H.; Djearamane, S.; Watanabe, A.; Aminuzzaman, M. Effect of calcination temperature on structural, morphological and optical properties of copper oxide nanostructures derived from *Garcinia mangostana* L. leaf extract. *Nanomaterials* **2022**, *12*, 3589. [[CrossRef](#)]
59. Sajjad, A.; Bhatti, S.H.; Ali, Z.; Jaffari, G.H.; Khan, N.A.; Rizvi, Z.F.; Zia, M. Photoinduced fabrication of zinc oxide nanoparticles: Transformation of morphological and biological response on light irradiance. *ACS. Omega.* **2021**, *6*, 11783–11793. [[CrossRef](#)]

60. Sharma, S.; Yadav, D.K.; Chawla, K.; Lai, N.; Lai, C. Synthesis and characterization of CuO nanoparticles by *Aloe barbadensis* leaves. *Quantum J. Eng. Sci. Technol.* **2021**, *2*, 1–9.
61. You, W.; Ahn, J.C.; Boopathi, V.; Arunkumar, L.; Rupa, E.J.; Akter, R.; Kong, B.M.; Lee, G.S.; Yang, D.C.; Kang, S.C.; et al. Enhanced antiobesity efficacy of tryptophan using the nanoformulation of *Dendropanax morbifera* extract mediated with ZnO nanoparticle. *Materials* **2021**, *14*, 824. [[CrossRef](#)]
62. Aminuzzaman, M.; Chong, C.-Y.; Goh, W.-S.; Phang, Y.-K.; Tey, L.-H.; Chee, S.-Y.; Akhtaruzzaman, M. Biosynthesis of NiO nanoparticles using soursop (*Annona muricata* L.) fruit peel green waste and their photocatalytic performance on crystal violet dye. *J. Clust. Sci.* **2021**, *32*, 949–958. [[CrossRef](#)]
63. Ramzan, M.; Obodo, R.M.; Mukhtar, S.; Ilyas, S.Z.; Aziz, F.; Thovhogi, N. Green synthesis of copper oxide nanoparticles using *Cedrus deodara* aqueous extract for antibacterial activity. *Mater. Today Proc.* **2021**, *36*, 576–581. [[CrossRef](#)]
64. Ahn, E.-Y.; Shin, S.-W.; Kim, K.; Park, Y. Facile green synthesis of titanium dioxide nanoparticles by upcycling mangosteen (*Garcinia mangostana*) pericarp extract. *Nanoscale Res. Lett.* **2022**, *17*, 40–51. [[CrossRef](#)]
65. Basavalingiah, K.R.; Harishkumar, S.; Udayabhanu; Nagaraju, G.; Rangappa, D. Chikkahanumantharayappa. Highly porous, honeycomb like Ag–ZnO nanomaterials for enhanced photocatalytic and photoluminescence studies: Green synthesis using *Azadirachta indica* gum. *SN Appl. Sci.* **2019**, *1*, 935. [[CrossRef](#)]
66. Mfon, R.E.; Hall, S.R.; Sarua, A. Effect of *Ocimum gratissimum* plant leaf extract concentration and annealing temperature on the structure and optical properties of synthesized zinc oxide nanoparticles. *Educ. J. Sci. Math. Technol.* **2020**, *7*, 1–13. [[CrossRef](#)]
67. Siddiqi, K.S.; Husen, A. Current status of plant metabolite-based fabrication of copper/copper oxide nanoparticles and their applications: A review. *Biomater. Res.* **2020**, *24*, 11. [[CrossRef](#)]
68. Karthiga, P.; Rajeshkumar, S.; Annadurai, G. Mechanism of larvicidal activity of antimicrobial silver nanoparticles synthesized using *Garcinia mangostana* bark extract. *J. Clust. Sci.* **2018**, *29*, 1233–1241. [[CrossRef](#)]
69. Das, S.; Srivastava, V.C. Synthesis and characterization of ZnO/CuO nanocomposite by electrochemical method. *Mater. Sci. Semicond. Process.* **2017**, *57*, 173–177. [[CrossRef](#)]
70. Georgia, B.J.; Gheena, S.; Pratibha, R.; Rajesh, K.S.; Kartikeyan, R.; Abilasha, R. Anticancer activity of green synthesized selenium nanoparticles from *Garcinia mangostana* crude extract against MCF-7 breast cancer cells. *J. Popul. Ther. Clin. Pharmacol.* **2023**, *30*, e74–e82. [[CrossRef](#)]
71. Yuan, L.-D.; Deng, H.-X.; Li, S.-S.; Wei, S.-H.; Luo, J.-W. Unified theory of direct or indirect band-gap nature of conventional semiconductors. *Phys. Rev. B* **2018**, *98*, 245203. [[CrossRef](#)]
72. Lany, S. Semiconducting transition metal oxides. *J. Phys. Condens. Matter.* **2015**, *27*, 283203. [[CrossRef](#)] [[PubMed](#)]
73. Rao, G.T.; Ravikumar, R.V.S.S.N. Novel Fe-doped ZnO-CdS nanocomposite with enhanced visible light-driven photocatalytic performance. *Mater. Res. Innov.* **2020**, *25*, 215–220. [[CrossRef](#)]
74. Fundamentals of Light-Emitting Diodes (LEDs). Available online: <https://zeiss-campus.magnet.fsu.edu/print/lightsources/leds-print.html#:~:text=However,%20most%20white%20light%20diodes,emission%20at%20a%20longer%20wavelength> (accessed on 9 January 2024).
75. Tan, Y.H.; Goh, P.S.; Lai, G.S.; Lau, W.J.; Ismail, A.F. Treatment of aerobic treated palm oil mill effluent (AT-POME) by using TiO₂ photocatalytic process. *J. Teknol.* **2014**, *70*, 61–63. [[CrossRef](#)]
76. Kanakaraju, D.; Ahmad, N.L.B.; Sedik, N.B.M.; Long, S.G.H.; Guan, T.M.; Chin, L.Y. Performance of solar photocatalysis and photo-fenton degradation of palm oil mill effluent. *Malays. J. Anal. Sci.* **2017**, *21*, 996–1007. [[CrossRef](#)]
77. Chai, H.Y.; Lam, S.M.; Sin, J.C. Green synthesis of ZnO nanoparticles using *Hibiscus rosa-sinensis* leaves extracts and evaluation of their photocatalytic activities. In Proceedings of the International Symposium on Green and Sustainable Technology (ISGST2019), Perak, Malaysia, 23–26 April 2019.
78. Lam, S.-M.; Wong, K.-A.; Sin, J.-C. Fabrication of flower-like ZnO micro/nanostructures for photodegradation of pre-treated palm oil mill effluent. *IOP Conf. Ser. Earth Environ. Sci.* **2018**, *112*, 012003–012007. [[CrossRef](#)]
79. Chan, Y.B.; Aminuzzaman, M.; Khalilur Rahman, M.; Win, Y.F.; Sultana, S.; Cheah, S.-Y.; Watanabe, A.; Wong, L.S.; Guha, S.M.; Djearamane, S.; et al. Green synthesis of ZnO nanoparticles using the mangosteen (*Garcinia mangostana* L.) leaf extract: Comparative preliminary in vitro antibacterial study. *Green Process. Synth.* **2024**, *13*, 20230251–20230270. [[CrossRef](#)]

Disclaimer/Publisher’s Note: The statements, opinions and data contained in all publications are solely those of the individual author(s) and contributor(s) and not of MDPI and/or the editor(s). MDPI and/or the editor(s) disclaim responsibility for any injury to people or property resulting from any ideas, methods, instructions or products referred to in the content.